

Domain-Invariant Similarity Activation Map Contrastive Learning for Retrieval-Based Long-Term Visual Localization

Hanjiang Hu, Hesheng Wang, *Senior Member, IEEE*, Zhe Liu, and Weidong Chen, *Member, IEEE*

Abstract—Visual localization is a crucial component in the application of mobile robot and autonomous driving. Image retrieval is an efficient and effective technique in image-based localization methods. Due to the drastic variability of environmental conditions, e.g., illumination changes, retrieval-based visual localization is severely affected and becomes a challenging problem. In this work, a general architecture is first formulated probabilistically to extract domain-invariant features through multi-domain image translation. Then, a novel gradient-weighted similarity activation mapping loss (Grad-SAM) is incorporated for finer localization with high accuracy. We also propose a new adaptive triplet loss to boost the contrastive learning of the embedding in a self-supervised manner. The final coarse-to-fine image retrieval pipeline is implemented as the sequential combination of models with and without Grad-SAM loss. Extensive experiments have been conducted to validate the effectiveness of the proposed approach on the CMU-Seasons dataset. The strong generalization ability of our approach is verified with the RobotCar dataset using models pre-trained on urban parts of the CMU-Seasons dataset. Our performance is on par with or even outperforms the state-of-the-art image-based localization baselines in medium or high precision, especially under challenging environments with illumination variance, vegetation, and night-time images. Moreover, real-site experiments have been conducted to validate the efficiency and effectiveness of the coarse-to-fine strategy for localization.

Index Terms—Deep representation learning, place recognition, visual localization.

I. INTRODUCTION

VISUAL localization is an essential problem in visual perception for autonomous driving and mobile robots [1]–[3], which is low-cost and efficient compared with global

Manuscript received September 23, 2020; revised October 25, 2020 and November 27, 2020; accepted December 6, 2020. Recommended by Associate Editor Long Chen. (*Corresponding author: Hesheng Wang.*)

Citation: H. J. Hu, H. S. Wang, Z. Liu, and W. D. Chen, “Domain-invariant similarity activation map contrastive learning for retrieval-based long-term visual localization,” *IEEE/CAA J. Autom. Sinica*, vol. 9, no. 2, pp. 313–328, Feb. 2022.

H. J. Hu and W. D. Chen are with the Department of Automation, Shanghai Jiao Tong University, Shanghai 200240, China (e-mail: huhanjiang@sjtu.edu.cn; wdchen@sjtu.edu.cn).

H. S. Wang is with the Department of Automation, Institute of Medical Robotics, Key Laboratory of System Control and Information Processing of Ministry of Education, Key Laboratory of Marine Intelligent Equipment and System of Ministry of Education, Shanghai Jiao Tong University, Shanghai 200240, China (e-mail: wanghesheng@sjtu.edu.cn).

Z. Liu is with the the Department of Computer Science and Technology, University of Cambridge, Cambridge CB3 0FD, United Kingdom (e-mail: z1457@cam.ac.uk).

Color versions of one or more of the figures in this paper are available online at <http://ieeexplore.ieee.org>.

Digital Object Identifier 10.1109/JAS.2021.1003907

positioning system-based (GPS-based) or light detection and ranging-based (LiDAR-based) localization methods. Image retrieval, i.e., recognizing the most similar place in the database for each query image [4]–[6], is a convenient and effective technique for image-based localization, which serves place recognition for loop closure and provides initial pose for finer 6-DoF camera pose regression [7], [8] for relocalization in simultaneous localization and mapping (SLAM).

However, the drastic perceptual changes caused by long-term environmental condition variance, e.g., changing seasons, illumination, and weather, casts serious challenges on image-based localization in long-term outdoor self-driving scenarios [9]. Traditional feature descriptors (SIFT, BRIEF, ORB, BRISK, etc.) can be only used for image matching under scenes without significant appearance changes due to the reliance on image pixels. With convolutional neural networks (CNNs) making remarkable progress in the field of computer vision and autonomous driving [10], learning-based methods have gained significant attention owing to the robustness of deep features against changing environments for place recognition and retrieval [11]–[13].

Contrastive learning is an important technique for image recognition tasks [14]–[16], also known as deep metric learning, which aims to learn metrics and latent representations with closer distance for similar images. Compared to face recognition, supervised learning for place recognition [13], [17] suffers from difficulty in determining which clip of images should be grouped to the same place in the sequence of continuous images. Moreover, supervised contrastive learning methods for outdoor place recognition [18], [19] need numerous paired samples for model training due to heterogeneously entangled scenes with multiple environmental conditions, which is costly and inefficient. Additionally, considering a feature map with salient areas in the explanation of CNNs for classification task [20]–[22], retrieval-based localization could be addressed through such attentive or contextual information [23], [24]. However, these methods have no direct access to the similarity of the extracted feature so they are not appropriate for high-precision localization.

To address these issues, we first propose an unsupervised and implicitly content-disentangled representation learning through probabilistic modeling to obtain domain-invariant features (DIF) based on multi-domain image translation with feature consistency loss (FCL). For retrieval with high accuracy, a novel gradient-weighted similarity activity

mapping (Grad-SAM) loss is introduced inside the training framework inspired by [20]–[22]. Furthermore, a novel unsupervised adaptive triplet loss is incorporated in the pipeline to promote the training of FCL or Grad-SAM and the two-stage test pipeline is implemented in a coarse-to-fine manner for the performance compensation and improvement. We further investigate the localization and place recognition performance of the proposed method by conducting extensive experiments on both CMU-Seasons dataset and RobotCar-Seasons dataset. Compared to state-of-the-art image-based baselines, our method presents competitive results in medium and high precision. In the real-site experiment, the proposed two-stage method is validated to be simultaneously time-efficient and effective. An example of image retrieval is shown in Fig. 1. Our contributions are summarized as follows:

1) A domain-invariant feature learning framework is proposed based on multi-domain image-to-image translation architecture with feature consistency loss and is statistically formulated as a probabilistic model of image disentanglement.

2) A new Grad-SAM loss is proposed inside the framework to leverage the localizing information of feature map for high-accuracy retrieval.

3) A novel adaptive triplet loss is introduced for FCL or Grad-SAM learning for the self-supervised contrastive learning and gives the effective two-stage retrieval pipeline from coarse to fine.

4) The effectiveness of the proposed approach is validated on CMU-Seasons dataset and RobotCar-Seasons dataset for visual localization through extensive experimentation. Our results are on par with state-of-the-art baselines of image retrieval-based localization for medium and high precision. Also, the time-efficiency and effectiveness of its applicability is shown through a real-site experiment as well.

The rest of this paper is organized as follows. Section II presents the related work in place recognition and representation learning for image retrieval. Section III presents the formulation of domain-invariant feature learning model with FCL. Section IV introduces the adaptive triplet loss and the two-stage retrieval pipeline with Grad-SAM loss. Section V shows the experimental results on visual localization benchmark. Finally, in Section VI we draw our conclusions and present some suggestions for the future work.

II. RELATED WORK

A. Place Recognition and Localization

Outdoor visual place recognition has been studied for many years for visual localization in autonomous driving or loop closure detection of SLAM, in which the most similar images are retrieved from key frame database for query images. Traditional feature descriptors have been used in traditional robotic applications [25], [26] and are aggregated for image retrieval and matching [27]–[30], which have successfully addressed most cases of loop closure detection in visual SLAM [31] without significant environmental changes. VLAD [32] is the most successful man-made feature for place recognition and has been extended to different versions. NetVLAD [4] extracts deep features through VLAD-like

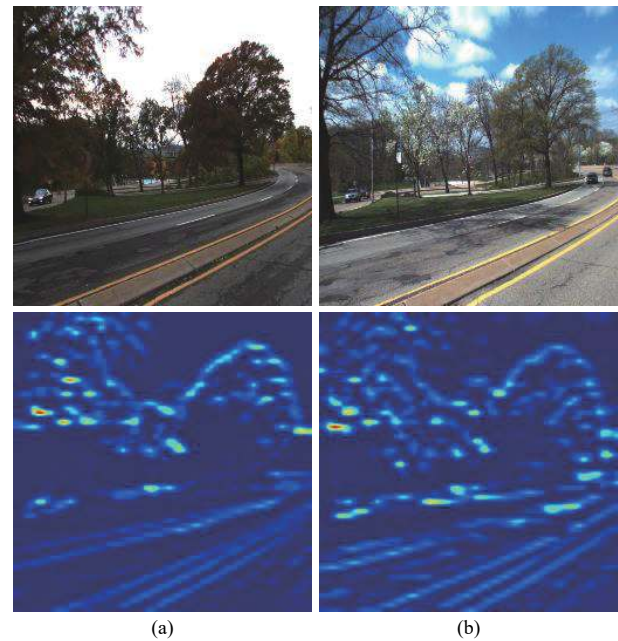


Fig. 1. On the first row, column (a) shows a query image under *Overcast + Mixed Foliage* condition and column (b) shows the retrieved image under *Sunny + No Foliage* condition. On the second row, the gradient-weighted similarity activation maps are shown for the above images. The activation map visualizes the salient area on the image which contributes most to the matching and retrieval across the different environments.

network architecture. DenseVLAD [6] presents impressive results through extracting multi-scale SIFT descriptor for aggregation under drastic perceptual variance. To reduce the false positive rates of single feature-based methods, sequence-based place recognition [33], [34] is proposed for real-time loop closure for SLAM.

Since convolutional neural networks (CNNs) has successfully addressed many tasks in computer vision [35], long-term visual place recognition and localization have significantly developed assisted along with CNNs [4], [13], [36]. Some solutions to the change of appearance are based on image translation [37]–[40], where images are transferred across different domains based on generative adversarial networks (GANs) [41], [42]. Porav *et al.* [43] first translates query images to database domain through CycleGAN [44] and retrieves target images through hand-crafted descriptors. ToDayGAN [45] similarly translates night-images to day-images and uses DenseVLAD for retrieval. Jenicek and Chum [36] proposes to use U-Net to obtain photometric normalization image and finds deep embedding for retrieval. However, generalization ability is limited by translation-based methods because the accuracy of retrieval on image level largely depends on the quality of the translated image compared to the retrieval with latent-feature.

Some other recent work follows the pipeline of learning the robust deep representation through neural networks together with semantic [46], [47], geometric [48], [49], context-aware information [23], [24], [50], [51], etc. Although these models can perform the image retrieval in the feature level, the representation features are trained with the aid of auxiliary

information which is costly to obtain in most cases. With the least human effort for auxiliary perception information and inspired by classification activation map [20]–[22] in visual explanation of CNN, we introduce the notion of activation map to the representation learning for fine place recognition, of which the necessity and advantages lie in implementing retrieval in the latent feature space with self-supervised attentive information without any human effort or laborious annotations.

B. Disentanglement Representation

Latent representation reveals the feature vectors in the latent space which determine the distribution of samples. Therefore, it is essential to find the latent disentangled representation to analyze the attributes of data distribution. A similar application is the latent factor model (LFM) in recommender systems [52]–[54], where the latent factor contributes to the preference of specific users. In the field of style transfer or image translation [37], [55], deep representations of images are modeled according to the variations of data which depend on different factors across domains [56], [57], e.g., disentangled content and style representation. Supervised approaches [58], [59] learn class-specific representations through labeled data, and many works have appeared to learn disentangled representation in unsupervised manners [60], [61]. Recently, fully- and partially-shared representation of latent space have been investigated for unsupervised image-to-image translation [39], [40]. Inspired by these methods, where the content code is shared across all the domains but the style code is domain-specific, our domain-invariant representation learning is probabilistically formulated and modeled as an extended and modified version of CycleGAN [44] or ComboGAN [38].

For the application of representation learning in place recognition under changing environments, where each environmental condition corresponds to one domain style and the images share similar scene content across different environments, it is appropriate to make the assumption of disentangled representation to this problem case. Recent works for condition-invariant deep representation learning [5], [62]–[64] in long-term changing environments mainly rely on variance-removal or other auxiliary information introduced in Section II-A. Reference [17] removes the dimension related to the changing condition through PCA for the deep embeddings of latent space through classification model. Reference [12] separates the condition-invariant representation from VLAD features with GANs across multiple domains. Reference [65] filters the distracting feature maps in the shallow CNNs but matches with deep features in deeper CNNs to improve condition- and viewpoint-invariance [66] using image pairs. Compared to these two-stage or supervised methods, we adopt domain-invariant feature learning methods [63], [64] which possess advantages on direct, low-cost, and efficient learning.

C. Contrastive Learning

Contrastive learning, a.k.a., deep metric learning [14], [67] stems from distance metric learning [68], [69] in machine learning but extracts deep features through deep neural

networks, i.e., learning appropriate embeddings and metrics for effective discrimination between similar sample pairs and different sample pairs. With the help of neural networks, deep metric learning typically utilizes siamese networks [70], [71] or triplet networks [72], [73], which makes the embedding of same category closer than that of different category with triple labeled input samples for face recognition, human re-identification, etc.

Coming to long-term place recognition and visual localization, many works have recently used supervised learning together with siamese networks and triplet loss [18], [62]. To avoid vanishing gradient of small distance from different pairs with triplet loss form [14], [15] proposes another form of triplet loss. Due to the hard-annotated data for supervised learning, Radenović *et al.* [19] proposes to leverage geometry of 3D model from structure-from-motion (SfM) for triplet learning in an automated manner. But SfM is off-line and costly, so it is not possible for end-to-end training. Instead we employ an unsupervised triplet training technique adapted to the DIFL framework [63] so that domain-invariant and scene-specific representation can be trained in an unsupervised and end-to-end way efficiently.

III. FORMULATION OF DOMAIN-INVARIANT FEATURE LEARNING

A. Problem Assumptions

Our approach to long-term visual place localization and recognition is modeled in the setting of multi-domain unsupervised image-to-image translation, where all query and database images are captured from multiple identical sequences across environments. Images in different environmental conditions belong to corresponding domains respectively. Let the total number of domains be denoted as N and two different domains are randomly sampled from $\{1, \dots, N\}$ for each translation iteration, e.g., $i, j \in \{1, \dots, N\}, i \neq j$. Let $x_i \in \mathcal{X}_i$ and $x_j \in \mathcal{X}_j$ represent images from these two domains. For the multi-domain image-to-image translation task [38], the goal is to find all conditional distributions $p(x_i|x_j), \forall i \neq j, i, j \in \{1, \dots, N\}$ with known marginal distribution of $p(x_i), p(x_j)$, and translated conditional distribution $p(x_{j \rightarrow i}|x_j), p(x_{i \rightarrow j}|x_i)$. Since different domains correspond to different environmental conditions, we suppose the conditional distribution $p(x_i|x_j)$ is monomodal and deterministic compared to multimodal distribution across only two domains in [40]. As N increases to infinity and becomes continuous, the multi-domain translation model covers more domains and can be regarded as a generalized multi-modal translation with limited domains.

Like the shared-latent-space assumption in the recent unsupervised image-to-image translation methods [39], [40], the content representation c is shared across different domains while the style latent variable s_i belongs to each specific domain. For the image joint distribution in one domain $x_i \in \mathcal{X}_i$, it is generated from the prior distribution of content and style, $x_i = G_i(s_i, c)$, and the content and style are independent of each other. Since the condition distribution $p(x_i|x_j)$ is deterministic, the style variable is only embodied

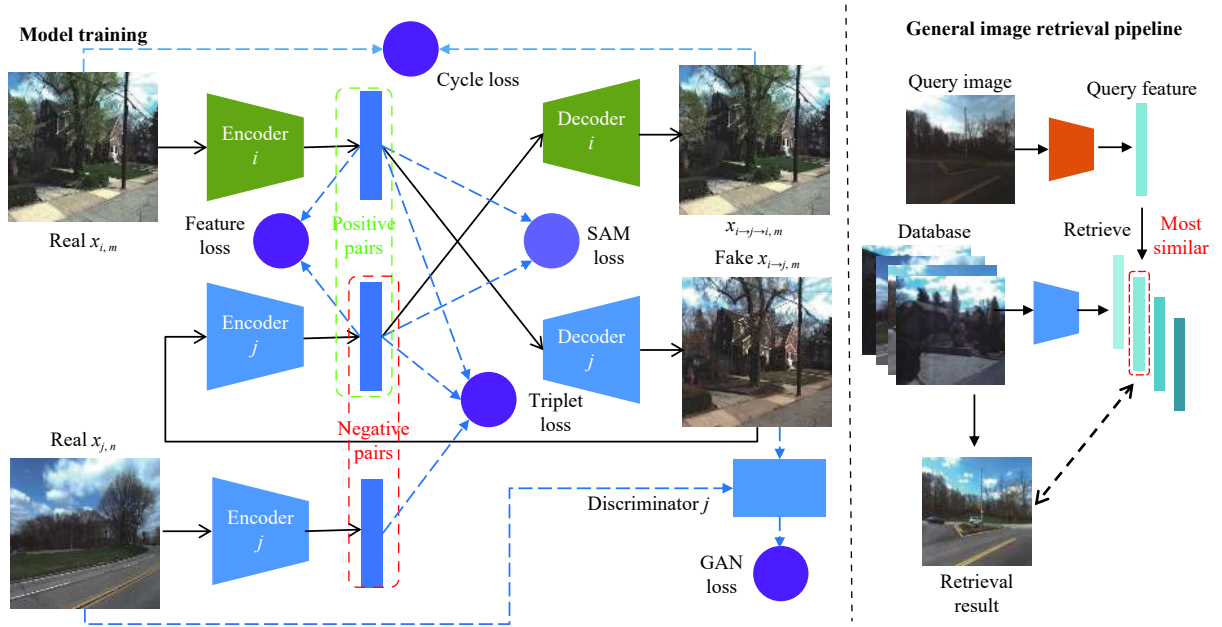


Fig. 2. The architecture overview for model training from domain i to j and general image retrieval pipeline while testing. The involved losses include GAN loss, cycle loss and feature loss, SAM loss, and triplet loss. Note that SAM loss are only used for fine model and the encoder, decoder and discriminator are specific for each domain.

in the latent generator of the specific domain, i.e., $x_i = G_i(s_i, c) = D_i^{c*}(c)$, $x_j = G_j(s_j, c) = D_j^{c*}(c)$. Under such assumptions, our method could be regarded as implicitly partially-shared, although only content latent code is explicitly found across multiple domains with corresponding generators. Following the previous work [40], we further assume that the domain-specific decoder functions for shared content code, D_i^{c*}, D_j^{c*} , are deterministic and their inverse encoder functions exist, where $E_i^{c*} = (D_i^{c*})^{-1}$, $E_j^{c*} = (D_j^{c*})^{-1}$. And our goal of domain-invariant representation learning is to find the underlying decoders D_i^{c*}, D_j^{c*} , and encoders E_i^{c*}, E_j^{c*} for all the environmental domains through neural networks, so that the domain-invariant latent code c could be extracted for any given image sample x_i through $c = E_i^{c*}(x_i)$. The overview architecture based on the assumption is shown in Fig. 2, of which the details are introduced in the Sections III and IV.

B. Model Architecture

We adopt the multi-domain image-to-image translation architecture [38], which is an expansion of CycleGAN [44] from two domains to multiple domains. The generator networks in the framework are decoupled into domain-specific pairs of encoders E_i^c and decoders D_i^c for any domain i . The encoder are the first half of the generator while the decoder is the second half for each domain. For image translation across multiple domains, the encoders and decoders can be randomly combined like manipulation of blocks. The discriminators D_i are also domain-specific for domain i and optimized in adversarial training as well. The detailed architectures of encoder, decoder, and discriminator for each domain is the same as ComboGAN [38]. Note that [63] applies the ComboGAN architecture for image retrieval with feature consistency loss, resulting in an effective self-supervised retrieval-based localization method. However, in

this section we further formulate the architecture in a probabilistic framework, combining the multi-domain image translation and domain-invariant representation learning.

For images in similar sequences under different environments, first suppose domain i, j are selected randomly and images are denoted as x_i, x_j . The basic framework DIFL is shown as Fig. 3, including GAN loss, cycle consistency loss and feature consistency loss. For the image translation pass from domain i to domain j , the latent feature is first encoded by encoder E_i^c and then decoded by decoder D_j^c . The translated image goes back through encoder E_j^c and decoder D_i^c to find the cycle consistency loss (1) [44]. Also, the translated image goes through the discriminator D_j to find adversarial loss (2) [41]. The pass from domain j to domain i is similar.

$$\mathcal{L}_{\text{Cycle}}^{x_i} = \mathbb{E}_{x_i \sim p(x_i)} [\| (D_i^c(E_j^c((D_j^c(E_i^c(x_i)))))) - x_i \|_1]. \quad (1)$$

The adversarial loss (2) makes the translated image $x_{i \rightarrow j}$ indistinguishable from the real image x_j and the distribution of translated images close to the distribution of real images.

$$\mathcal{L}_{\text{GAN}}^{x_i} = \mathbb{E}_{x_j \sim p(x_j)} [(D_j(x_j) - 1)^2] + \mathbb{E}_{x_i \sim p(x_i)} [D_j(D_j^c(E_i^c(x_i)))^2]. \quad (2)$$

The cycle consistency loss (1) originates from CycleGAN [44], which has been proved to infer deterministic translation [40] and is suitable for representation learning through image translation among multiple domains. For the pure multi-domain image translation task, i.e., ComboGAN [38], the total ComboGAN loss only contains adversarial loss and cycle consistency loss.

$$\mathcal{L}_{\text{ComboGAN}} = \mathcal{L}_{\text{GAN}}^{x_i} + \mathcal{L}_{\text{GAN}}^{x_j} + \lambda_{\text{cyc}} (\mathcal{L}_{\text{Cycle}}^{x_i} + \mathcal{L}_{\text{Cycle}}^{x_j}). \quad (3)$$

Since every domain owns a set of encoder, decoder, and discriminator, the total architecture is complicated and can be

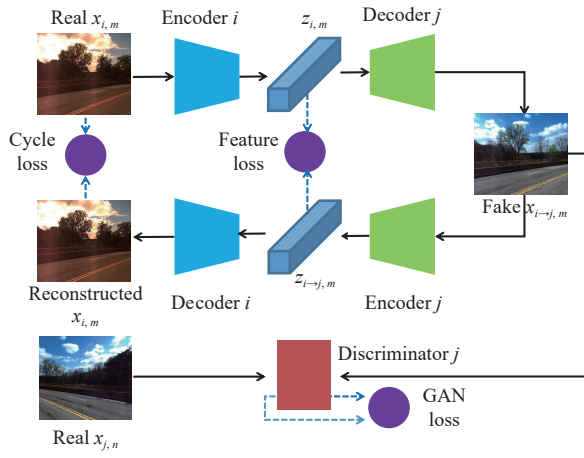


Fig. 3. Network architecture for image translation from domain i to j . Constraint by GAN loss, cycle loss, and feature loss, the latent feature code is the domain-invariant representation. The discriminator D_j results in GAN loss through adversarial training, given the real image of domain j and the translated image from domain i to j .

modeled through a probabilistic graph if all the encoders and decoders are regarded as conditional probability distribution. Supposing the optimality of ComboGAN loss (3) is reached, the complex forward propagation during training can be simplified and the representation embedding can be analyzed.

Without loss of generality, image $x_{i,m}, x_{j,n}$ are selected from image sequences $x_i, x_j, i \neq j$, where m, n represent the places of the shared image sequences and only related to the content of images. According to the assumptions in Section III-A, m, n represent the shared domain-invariant content latent code c across different domains. For the translation from image $x_{i,m}$ to domain j , we have

$$z_{i,m} = E_i^c(x_{i,m}) \quad (4)$$

$$x_{i \to j, m} = D_j^c(z_{i,m}) \quad (5)$$

$$z_{i \to j, m} = E_j^c(x_{i \to j, m}) \quad (6)$$

$$x_{i,m} = D_i^c(z_{i \to j, m}). \quad (7)$$

The latent code $z_{i,m}$ implies the relationship of domain i and the content of image m from (4). Due to the adversarial loss (2), the translated image $x_{i \to j, m}$ has the same distribution as image $x_{j,n}$, i.e., $x_{i \to j, m}, x_{j,n} \sim p(x_j)$. For the reconstructed image from (7), the cycle consistency loss (1) limits it to the original image $x_{i,m}$.

From (4) and (5), we have

$$p(x_{i \to j, m}) = p(x|z_{i,m}, D_j^c) = p(x_{j,m}) \quad (8)$$

which indicates $x_{i \to j, m}$ and i are independent if the optimality of adversarial loss (2) is reached, and $z_{i \to j, m}$ and i are also independent from (6). Similarly, $z_{i,m}$ and j are independent for any $j \neq i$. Combining (5), (6) and (4), (7), we can find the relationship between $z_{i,m}$ and $z_{i \to j, m}$ and the weak form of inverse constraint on encoders and decoders below:

$$z_{i \to j, m} = E_j^c(D_j^c(z_{i,m})) \quad (9)$$

$$z_{i,m} = E_i^c(D_i^c(z_{i \to j, m})) \quad (10)$$

$$E_i^c(D_i^c) = (E_j^c(D_j^c))^{-1}, \forall i \neq j. \quad (11)$$

When the optimality of original ComboGAN loss (3) is reached, for any $i \neq j$, the latent code $z_{i,m}$ and $z_{i \to j, m}$ are not related to j and i , respectively, which is consistent with the proposition that cycle consistency loss cannot infer shared-latent learning in [39]. Consequently, the representation embeddings are not domain-invariant and not appropriate for image retrieval, and the underlying inverse encoders and decoders have not been found through the vanilla ComboGAN image translation model.

C. Feature Consistency Loss

To obtain the shared-latent feature across different domains, unlike [39], we use an additional loss exerted on the latent space called the feature consistency loss as proposed in [63]. Under the above assumptions, for image x_i from domain i it is formulated as

$$\mathcal{L}_{\text{FCL}}^{x_i} = \mathbb{E}_{x_i \sim p(x_i)} [\|E_j^c((D_j^c(E_i^c(x_i)))) - E_i^c(x_i)\|_2]. \quad (12)$$

As a result, the domain-invariant feature [63] can be extracted by combining all the weighted losses together

$$\begin{aligned} \mathcal{L}_{\text{DIF}} = & \mathcal{L}_{\text{GAN}}^{x_i} + \mathcal{L}_{\text{GAN}}^{x_j} + \lambda_{\text{cyc}}(\mathcal{L}_{\text{Cycle}}^{x_i} + \mathcal{L}_{\text{Cycle}}^{x_j}) \\ & + \lambda_{\text{FCL}}(\mathcal{L}_{\text{FCL}}^{x_i} + \mathcal{L}_{\text{FCL}}^{x_j}). \end{aligned} \quad (13)$$

Here gives the theoretical analysis for FCL. Supposing the optimality of the DIF loss (13) is reached, (4)–(11) are still satisfied. Additionally, because of the feature consistency loss (12), based on (4), (6), (10), we have

$$z_{i \to j, m} = z_{i,m} \quad (14)$$

$$E_i^c = (D_i^c)^{-1}. \quad (15)$$

Since $z_{i \to j, m}$ and i are independent (as discussed in the previous section), $z_{i,m}$ and i are independent for any domain i from (14), which indicates that the latent feature is well-shared across multiple domains and represents the content latent code given any image from any domain. Furthermore, the trained encoders and decoders are inverse and the goal of finding underlying encoders E_i^{c*} and decoders D_i^{c*} is reached according to Section III-A. So it is appropriate to use the content latent code for image representation across different environmental conditions.

IV. COARSE-TO-FINE RETRIEVAL-BASED LOCALIZATION

A. Gradient-Weighted Similarity Activation Mapping Loss

The original domain-invariant feature (13) cannot excavate the context or localizing information of the content latent feature map; as a result the performance of place recognition under high accuracy is limited. To this end, we propose a novel gradient-weighted similarity activation mapping loss for shared-latent feature to fully discover the weighted similar area for high-accuracy retrieval.

Inspired by CAM [20], Grad-CAM [21], and Grad-CAM++ [22] in visual explanation for classification with convolutional neural networks, we assume that the place recognition task

can be regarded as an extension of image multi-classification with infinite target classes, where each database image represents a single target class for each query image during the retrieval process. Then, for each query image, the similarity to each database image is treated as the score before softmax or probability for multi-classification task and the one with the largest similarity is the retrieved result, which is similar to the classification result with the largest probability.

Ideally, suppose the identical content latent feature maps from domain i, j , $z_{i,m}, z_{j,m}$, have the shape of $n \times h \times w$, where identical content m is omitted for brevity. First the mean value of the cosine similarity on the height and width dimension is calculated below:

$$Y = \frac{1}{n} \sum_k \times \frac{\sum_p \sum_q z_i^{kpq} z_j^{kpq}}{\sqrt{\sum_{p,q} z_i^{kpq^2}} \sqrt{\sum_{p,q} z_j^{kpq^2}}} \quad (16)$$

where z_i^{kpq} represents the k th, p th, and q th on the dimension of channel, height and width, i.e., $n \times h \times w$ for the content feature map z_i .

Y is the score of similarity between z_i and z_j . Following the definition of Grad-CAM [21], we have the similarity activation weight and map:

$$\omega_{i,j}^k = \sum_p \sum_q \frac{\partial Y}{\partial z_i^{kpq}} \quad (17)$$

$$L_{i,j}^{pq} = ReLU\left(\sum_k \omega_{i,j}^k z_i^{kpq}\right) \quad (18)$$

where $\omega_{i,j}^k$ is the weight that z_j^k gives to z_i^k and $L_{i,j}^{pq}$ is the activation map of z_i^k at the position (p, q) given the database reference of z_j^k . z_j is treated as database feature ("class label") for the query feature z_i in the place recognition task. If we take partial derivative w.r.t. z_j^{kpq} in (17), the weight $\omega_{i,j}^k$ and the activation map $L_{i,j}^{pq}$ would result in that z_i is the retrieval from database under domain i given query feature z_j . $L_{i,j}^{pq}$ is unequal to $L_{j,i}^{pq}$ due to the different weight in (17). We denote $L_{i,j}$ as L_i and $L_{j,i}$ as L_j for short in the following notation.

Equations (17) and (18) are the mathematic formulation of the proposed Grad-SAM, where the activation map is aggregated by each gradient-weighted feature map, retaining the localizing information of the deep feature map. In order to only input the positively-activated areas for training, we exert a $ReLU$ function to obtain the final activation map $L_{i,j}$ or $L_{j,i}$.

Particularly, as shown in Fig. 4, inside the unsupervised DIFL architecture, the content latent codes $z_{i,m}, z_{j,m}$ are shared from the same distribution but $z_{i,m} \neq z_{j,m}$ for the unpaired $m \neq n$. The similarity activation map $L_{i,m}, L_{i \rightarrow j,m}$ could be visualized by resizing to the original size in Fig. 4. According to FCL loss (12), $z_{i,m}$ and $z_{i \rightarrow j,m}$ tend to be identical, which means that the calculation of similarity between them is meaningful and so is the SAM loss. Therefore, the self-supervised Grad-SAM loss for domain i could be formulated below based on (16)–(18):

$$\mathcal{L}_{SAM}^{x_i} = \mathbb{E}_{x_i \sim p(x_i)} [\|L_{i,m} - L_{i \rightarrow j,m}\|_2] \quad (19)$$

where $z_{i,m}$ and $z_{i \rightarrow j,m}$ are substituted into z_i and z_j in (16)–(18) and $L_{i,m}$ and $L_{i \rightarrow j,m}$ are short for $L_{i,j,m}$ and $L_{i \rightarrow j,i,m}$ derived from (17) and (18).

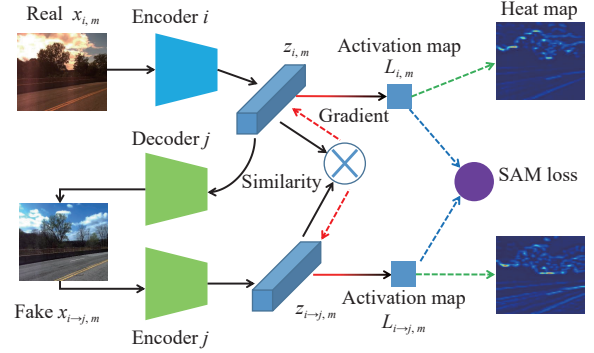


Fig. 4. The illustration of one branch of SAM loss from domain i to j . The real image in domain i is first translated to fake image in domain j , and the gradient of similarity w.r.t. each other could be calculated, denoted as red dashed lines. And then the activation map is the sum of feature map weighted by the gradient, shown as color-gradient line from red to black, and SAM loss could be calculated in a self-supervised manner. Note that the notation of $L_{i,m}$ and $L_{i \rightarrow j,m}$ here are short for $L_{i,j,m}$ and $L_{i \rightarrow j,i,m}$ derived from (17) and (18).

B. Adaptive Triplet Loss

Though the domain-invariant feature learning is obtained through feature consistency loss (12) and Grad-SAM loss (19) is for further finer retrieval with salient localizing information on the latent feature map, it is difficult to distinguish different latent content codes using domain-invariant features without explicit metric learning. As the distance of the latent features with the same content is decreasing due to feature consistency loss (12) and Grad-SAM loss (19), the distance of latent features for different contents may be forced to diminish as well, resulting in mismatched retrievals for test images in long-term visual localization.

Toward this end, we propose a novel adaptive triplet loss based on feature consistency loss (12) and Grad-SAM loss (19) to improve the contrastive learning of the latent representation inside the self-supervised DIFL framework. Suppose unpaired images $x_{i,m}, x_{j,n}$ are selected from domain $i, j, i \neq j$, where m, n represent the content of images. Note that for the purpose of unsupervised training pipelines, one of the selected image is horizontally flipped while the other is not so that $m \neq n$ is assured for the negative pair. The operation of flipping only one of the input images is random and also functions as data augmentation due to the fact that the flipped images follow the distribution of original images. Details could be found in Section V-A. For the self-supervised contrastive learning, the positively paired samples are not given but generated from the framework in (4)–(6) and (16)–(18), i.e., $z_{i,m}, z_{i \rightarrow j,m}$ and $L_{i,m}, L_{i \rightarrow j,m}$. For the negatively paired samples, for the sake of the fact that the images under the same environmental condition tend to be closer than ones under different conditions, the stricter constraint is implemented for negative pairs with the translated image and the other real image, which are under the same environment

but different places, i.e., $z_{i \rightarrow j,m}, z_{j,n}$ and $L_{i \rightarrow j,m}, L_{j,n}$.

Moreover, in order to improve the efficiency of the triplet loss for representation learning during the late iterations, the negative pair with the least distance between the original and the translated one is automatically selected as the hard negative pair $z_{j,n}^*$ or $L_{j,n}^*$ from a group of random negative candidates $Z_{j,n}$ or $L_{j,n}$, shown as (20) and (21). The adaptive triplet loss is calculated through these hard negative pairs without any supervision or extra priority information.

$$z_{j,n}^* = \arg \min_{z_{j,n} \in Z_{j,n}} \|z_{i \rightarrow j,m} - z_{j,n}\|_2 \quad (20)$$

$$L_{j,n}^* = \arg \min_{L_{j,n} \in L_{j,n}} \|L_{i \rightarrow j,m} - L_{j,n}\|_2. \quad (21)$$

We adopt the basic form of triplet loss from [15], but the *margin* depends on the feature consistency loss (12) or Grad-SAM loss (19), which adapts to the representation learning of (12) or (19). The illustrations of the adaptive triplet loss for FCL and SAM are shown in Figs. 5 and 6. The adaptive triplet loss for FCL and Grad-SAM for domain i is shown below:

$$\mathcal{L}_{\text{Triplet_FCL}}^{x_i} = \mathbb{E}_{x_i \sim p(x_i)} [\max(0, 1 - \frac{\|z_{i \rightarrow j,m} - z_{j,n}^*\|_2}{\|z_{i,m} - z_{i \rightarrow j,m}\|_2 + m_f \exp(-\alpha_f \|z_{i,m} - z_{i \rightarrow j,m}\|_2)})] \quad (22)$$

$$\mathcal{L}_{\text{Triplet_SAM}}^{x_i} = \mathbb{E}_{x_i \sim p(x_i)} [\max(0, 1 - \frac{\|L_{i \rightarrow j,m} - L_{j,n}^*\|_2}{\|L_{i,m} - L_{i \rightarrow j,m}\|_2 + m_s \exp(-\alpha_s \|L_{i,m} - L_{i \rightarrow j,m}\|_2)})] \quad (23)$$

where hyperparameters m_f, m_s are the *margin*, which is the value that the distance of negative pairs exceeds the distance of self-generated positive pairs when the image translation is well trained, i.e., $p(x_{i \rightarrow j,m}) = p(x_{j,m})$. However constant *margin* has an influence on the joint model training with FCL or Grad-SAM loss, so we propose the self-adaptive term, which is the exponential function of negative FCL loss or Grad-SAM loss weighted by α_f or α_s .

Combining with the adaptive triplet loss (22) or (23), in the beginning of the whole model training, the exponential adaptive term is close to 0 so the triplet loss term does not affect the FCL (12) or Grad-SAM (19). But as the training process goes by, the triplet loss would dominate the model training since the exponential adaptive term becomes larger and closer to 1.

C. Coarse-to-Fine Image Retrieval Pipeline

Different applications have different requirements for coarse- or high-precision localization, e.g., loop closure and relocalization in SLAM and 3D reconstruction. As shown in the Section III-C, the feature consistency loss together with the cycle consistency loss and GAN loss in image-to-image translation contribute to the domain-invariant representation learning architecture, where the latent feature is independent of the multiple environmental domains so that the feature could be used for image representation and retrieval across different environments. While the Grad-SAM loss in Section

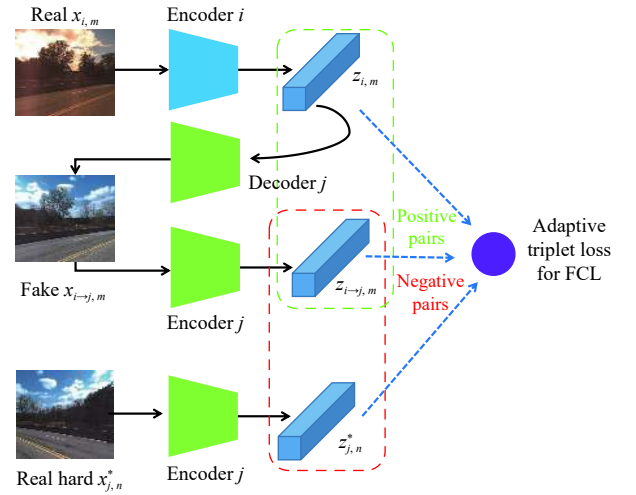


Fig. 5. The illustration of one-branch adaptive triplet loss for FCL from domain i to j . The inputs of the loss are the encoded latent features from real images in domain i, j and the translated image $i \rightarrow j$, resulting in the negative pairs with the red dashed box and the positive pairs with the green dashed box. Note that positive pairs only differ in the environment while the place is the only difference for the negative pairs.

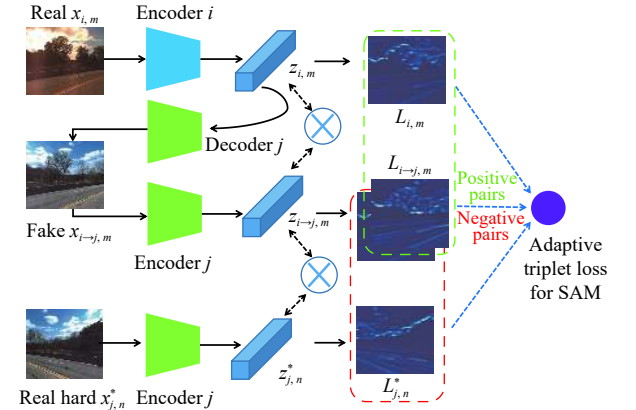


Fig. 6. The illustration of one-branch adaptive triplet loss for Grad-SAM from domain i to j . The inputs of the loss are the similarity activation maps from real images in domain i, j and the translated image $i \rightarrow j$. The negative pairs are bounded with the red dashed box while the positive pairs are bounded with the green dashed box. Note that the activation maps in domain i from two pairs are slightly different.

IV-A is incorporated to the basic architecture for the purpose of learning salient area and attentive information from the original latent feature, which is important to the high-precision retrieval. The adaptive triplet loss in Section IV-B can balance the self-supervised representation learning and feature consistency loss, which improves the retrieval results through ablation studies in Section V-D.

For the image retrieval, we adopt the coarse-to-fine strategy to fully leverage the models with different training settings for different specific purposes. The DIFL model with FCL (12) and triplet loss (22) aims to find the database retrieval for the query image using general domain-invariant features and results in better performance of localization within larger error thresholds, shown in Section V-D, which gives a good initial

TABLE I
ABLATION STUDY ON DIFFERENT STRATEGIES AND LOSS TERMS

Strategy	Flipped Negative	Hard Negative	FCL	Triplet FCL Margin	SAM	Triplet SAM Margin	Urban (%) 0.25 m / 0.5 m / 5 m 2° / 5° / 10°	Suburban (%) 0.25 m / 0.5 m / 5 m 2° / 5° / 10°	Park (%) 0.25 m / 0.5 m / 5 m 2° / 5° / 10°
Coarse-only	✓	×	✓	Adaptive	×	×	20.0 / 44.8 / 88.7	9.8 / 25.3 / 77.1	11.1 / 28.7 / 78.5
	×	✓	✓	Adaptive	×	×	19.9 / 44.6 / 87.8	9.7 / 24.6 / 74.2	10.8 / 27.5 / 76.4
	✓	✓	×	×	×	×	19.8 / 44.1 / 85.8	9.0 / 23.2 / 66.9	10.0 / 26.3 / 69.6
	✓	✓	✓	×	×	×	19.8 / 44.3 / 86.8	9.2 / 23.5 / 69.4	10.1 / 26.5 / 71.6
	✓	✓	✓	Constant	×	×	20.0 / 44.7 / 88.5	9.7 / 25.3 / 77.5	11.2 / 28.6 / 78.3
	✓	✓	✓	Adaptive	×	×	20.1 / 45.0 / 89.9	9.9 / 25.6 / 78.6	11.3 / 29.1 / 80.1
Fine-only	✓	×	✓	×	✓	Adaptive	22.3 / 45.6 / 83.6	10.9 / 26.0 / 68.6	12.8 / 30.9 / 73.4
	×	✓	✓	×	✓	Adaptive	21.8 / 45.1 / 82.4	10.6 / 25.4 / 67.5	12.1 / 29.6 / 72.3
	✓	✓	✓	×	✓	×	21.2 / 44.8 / 80.6	10.0 / 24.1 / 65.8	11.1 / 27.9 / 68.3
	✓	✓	✓	×	✓	Constant	22.3 / 45.5 / 83.7	11.0 / 26.0 / 68.4	12.9 / 30.9 / 73.2
	✓	✓	✓	×	✓	Adaptive	22.5 / 46.0 / 84.6	11.1 / 26.9 / 69.8	13.0 / 31.5 / 74.7
	✓	✓	✓	Adaptive	✓	Adaptive	22.7 / 46.4 / 85.4	11.3 / 27.2 / 71.9	13.2 / 32.2 / 76.9
Coarse-to-fine	✓	✓	✓	Adaptive	✓	Adaptive	22.6 / 47.3 / 89.1	11.1 / 27.5 / 77.6	12.6 / 31.3 / 80.0

range of retrieved candidates and can be used as a coarse retrieval.

The total loss for coarse-retrieval model training is shown below:

$$\begin{aligned} \mathcal{L}_{\text{coarse}} = & \mathcal{L}_{\text{GAN}}^{x_i} + \mathcal{L}_{\text{GAN}}^{x_j} + \lambda_{\text{cyc}}(\mathcal{L}_{\text{Cycle}}^{x_i} + \mathcal{L}_{\text{Cycle}}^{x_j}) \\ & + \lambda_{\text{FCL}}(\mathcal{L}_{\text{FCL}}^{x_i} + \mathcal{L}_{\text{FCL}}^{x_j}) \\ & + \lambda_{\text{Triplet_FCL}}(\mathcal{L}_{\text{Triplet_FCL}}^{x_i} + \mathcal{L}_{\text{Triplet_FCL}}^{x_j}) \end{aligned} \quad (24)$$

where λ_{cyc} , λ_{FCL} , and $\lambda_{\text{Triplet_FCL}}$ are the hyperparameters to weigh different loss terms.

Furthermore, to obtain the finer retrieval results, we incorporate the Grad-SAM (19) with its triplet loss (23) into the coarse-retrieval model, which fully digs out the localizing information of feature map and promotes the high-accuracy retrieval across different conditions shown in Table I. However, according to Section V-D, the accuracy of low-precision localization for fine-retrieval model is lower than the coarse-retrieval model, which shows the initial necessity of the coarse retrieval. The total loss for the finer model training is shown below:

$$\begin{aligned} \mathcal{L}_{\text{fine}} = & \mathcal{L}_{\text{GAN}}^{x_i} + \mathcal{L}_{\text{GAN}}^{x_j} + \lambda_{\text{cyc}}(\mathcal{L}_{\text{Cycle}}^{x_i} + \mathcal{L}_{\text{Cycle}}^{x_j}) \\ & + \lambda_{\text{FCL}}(\mathcal{L}_{\text{FCL}}^{x_i} + \mathcal{L}_{\text{FCL}}^{x_j}) + \lambda_{\text{SAM}}(\mathcal{L}_{\text{SAM}}^{x_i} + \mathcal{L}_{\text{SAM}}^{x_j}) \\ & + \lambda_{\text{Triplet_SAM}}(\mathcal{L}_{\text{Triplet_SAM}}^{x_i} + \mathcal{L}_{\text{Triplet_FCL}}^{x_j}) \\ & + \lambda_{\text{Triplet_FCL}}(\mathcal{L}_{\text{Triplet_FCL}}^{x_i} + \mathcal{L}_{\text{Triplet_FCL}}^{x_j}) \end{aligned} \quad (25)$$

where λ_{cyc} , λ_{FCL} , λ_{SAM} , $\lambda_{\text{Triplet_SAM}}$, and $\lambda_{\text{Triplet_FCL}}$ are the hyperparameters for each loss term.

Once the coarse and fine models are trained, the test pipeline contains coarse retrieval and finer retrieval. The 6-DoF poses of database images are given while the goal is to find the poses of query images. We first pre-encode each database image under the reference environment into feature maps through coarse model off line, forming the database of coarse features. While testing, for every query image, we extract the feature map using coarse encoder of the

corresponding domain and retrieve the $\text{top-}N$ most similar ones from pre-encoded coarse features in the database. The N candidates are then encoded through the fine model to find the secondary feature maps, and the query image is also encoded through the fine model to find the query feature. The most similar one in the N candidates is retrieved as the final result for localization. Although the coarse-to-fine strategy may not get the most similar retrieval globally in some cases, it will increase the accuracy within coarse error in Section V-D compared to the only single fine model, which is beneficial to the application of pose regression for relocalization. It may also benefit from the filtered coarse candidates in some cases, as in Table I, to improve medium-precision results. The 6-DoF pose of query image is the same as the finally-retrieved one in the database.

V. EXPERIMENTAL RESULTS

We conduct a series of experiments on CMU-Seasons dataset and validate the effectiveness of coarse-to-fine pipelines with the proposed FCL loss, Grad-SAM loss and adaptive triplet loss. With the model only trained on the urban parts of the CMU seasons dataset in an unsupervised manner, we compare our results with several image-based localization baselines on the untrained suburban and park parts of the CMU-Seasons dataset and RobotCar-Seasons dataset, showing the advantage under scenes with massive vegetation and robustness to huge illumination change. To prove the practical validity and applicability for mobile robotics, we have also conducted real-site field experiments under different environments with more angles using a mobile robot with camera and RTK-GPS. We conduct these experiments on two NVIDIA 2080Ti cards with 64 G RAM on Ubuntu 18.04 system. Our source code and pre-trained models are available on <https://github.com/HanjiangHu/DISAM>.

A. Experimental Setup

The first series of experiments are conducted on the CMU-

Seasons dataset [9], which is derived from the CMU Visual Localization [75] dataset. It was recorded by a vehicle with left-side and right-side cameras over a year along a route roughly 9 kilometers long in Pittsburgh, U.S. The environmental change of seasons, illumination, and especially foliage is very challenging on this dataset. Reference [9] benchmarks the dataset and presents the groundtruth of camera pose only for the reference database images, adding new categories and area divisions of the original dataset as well. There are 31 250 images in 7 slices for urban area, 13 736 images in 3 slices for suburban area, and 30 349 images in 7 slices for park area. Each area has only one reference and eleven query environmental conditions. The condition of database is *Sunny + No Foliage*, and conditions of query images could be any weather intersected with vegetation condition, e.g., *Overcast + Mixed Foliage*. Since the images in the training dataset contain both left-side and right-side ones, the operation of flipping horizontally is reasonable and acceptable for the unsupervised generation of negative pairs and data augmentation, as introduced in Section IV-B.

The second series of experiments are conducted on RobotCar-Seasons dataset [9] derived from Oxford RobotCar dataset [76]. The images were captured with three Point Grey Grasshopper2 cameras on the left, rear, and right of the vehicle along a 10 km route under changing weather, season, and illumination across a year in Oxford, U.K. It contains 6 95 4 triplets for database images under overcast condition, 3 100 triplets for day-time query images under 7 conditions, and 878 triplets for night-time images under 2 conditions. In the experiment we only test rear images with the pre-trained model on the urban part of CMU-Seasons dataset to validate the generalization ability of our approach. Considering that not all conditions of RoborCar datasets have exactly corresponding conditions in CMU-Seasons, we choose the pre-trained models under the conditions with the most similar descriptions and dates from CMU-Seasons dataset for all the conditions in RobotCar dataset listed in Table II. Note that for the conditions which are not included in CMU-Seasons, we use

TABLE II
CONDITION CORRESPONDENCE FOR ROBORCAR DATASET

Conditions in RobotCar		The most similar conditions in CMU-Seasons	
Description	Date	Description	Date
Overcast (reference)	28 Nov	Overcast, Mixed Foliage	28 Oct
Dawn	16 Dec	Low Sun, Mixed Foliage	12 Nov
Dusk	20 Feb	Low Sun, Foliage	4 Mar
Night	10 Dec	Overcast, Mixed Foliage	28 Oct
Night-rain	17 Dec	Overcast, Mixed Foliage	28 Oct
Overcast-summer	22 May	Overcast, Foliage	28 Jul
Overcast-winter	13 Nov	Cloudy, Foliage	1 Oct
Rain	25 Nov	Cloudy, Mixed Foliage	22 Nov
Snow	3 Feb	Low Sun, Snow	21 Dec
Sun	10 Mar	Sunny	4 Apr

the pre-trained models under the reference condition instead, *Overcast + Mixed Foliage*, for the sake of fairness.

The images are scaled to 286×286 and cropped to 256×256 randomly while training but directly scaled to 256×256 while testing, leading to a feature map with the shape of $256 \times 64 \times 64$. We follow the protocol introduced in [9] which is the percentage of correctly-localized query images. Since we only focus on high and medium precision, the pose error thresholds are $(0.25 \text{ m}, 2^\circ)$ and $(0.5 \text{ m}, 5^\circ)$ while coarse-precision (low-precision) $(5 \text{ m}, 10^\circ)$ is omitted for the purpose of high-precision localization except for the ablation study. We choose several image-based localization methods FAB-MAP [74], DIFL-FCL [63], NetVLAD [4], and DenseVLAD [6], which are the best image-based localization methods.

B. Evaluation on CMU-Seasons Dataset

Following the transfer learning strategy for DIFL in [63], we fine-tune the pre-trained models in [63] at epoch 300 which are trained only with cycle consistency loss and GAN loss under all the images from the CMU-Seasons dataset for pure image translation task. Then, for the representation learning task, the model is fine-tuned with images from Urban areas in an unsupervised manner, without paired images across conditions. After adding the other loss terms in (24) or (25), we continue to train until epoch 600, with a learning rate linearly decreasing from 0.0002 to 0. Then the model is trained in the same manner until epoch 1200 with split 300 epochs. In order to speed up and stabilize the training process with triplet loss, we use the random negative pairs from epoch 300 to epoch 600 for the fundamental representation learning and adopt the hard negative pairs from epoch 600, as shown in Section IV-B. We choose the hard negative pair from 10 pairs of negative samples for each iteration.

For the coarse-retrieval model training, the weight hyperparameter are maximumly set as $\lambda_{\text{cyc}} = 10, \lambda_{\text{FCL}} = 0.1$, and $\lambda_{\text{Triplet_FCL}} = 1$, which are all linearly increasing from 0 as the training process goes by to balance the multi-task framework. Similarly for the fine-retrieval model training, we set $\lambda_{\text{cyc}} = 10, \lambda_{\text{FCL}} = 0.1, \lambda_{\text{SAM}} = 1000, \lambda_{\text{Triplet_SAM}} = 1$, and $\lambda_{\text{Triplet_FCL}} = 1$ with a similar training strategy. The fine model consists of the metrics of both $L2$ and *cosine similarity* for FCL terms while only $L2$ metric is used in the coarse model for FCL terms. For the adaptive triplet loss, we set $m_f = 5, \alpha_f = 2$ in triplet FCL loss (22) and $m_s = 0.1, \alpha_s = 1000$ in triplet SAM loss (23). And during the two-stage retrieval, the number of coarse candidates *top-N* is set to be 3, which makes it both efficient and effective. In the two-stage retrieval pipeline, we use the mean value of the *cosine similarity* on the height and width dimension as the metric during the coarse retrieval, as shown in (16). For the fine retrieval, we use the normal *cosine similarity* for the flatten secondary features due to the salient information in the feature map.

Our final result is compared with baselines shown as Table III, which shows that ours outperforms baseline methods for high- and medium-precision localization, $(0.25 \text{ m}, 2^\circ)$ and $(0.5 \text{ m}, 5^\circ)$, in park and suburban area, which shows powerful generalization ability because the model is only trained on the

TABLE III
RESULTS COMPARISON TO BASELINES ON CMU-SEASONS DATASET

Method	Park (%) 0.25 m / 0.5 m 2° / 5°	Suburban (%) 0.25 m / 0.5 m 2° / 5°	Urban (%) 0.25 m / 0.5 m 2° / 5°
FAB-MAP [74]	0.8 / 1.7	0.5 / 1.5	2.7 / 6.4
NetVLAD [4]	5.6 / 15.7	7.7 / 21.0	17.4 / 40.3
DenseVLAD [6]	10.3 / 27.1	9.8 / 26.6	22.2 / 48.6
DIFL-FCL [63]	11.4 / 28.9	9.7 / 25.0	20.2 / 44.7
Coarse-only (ours)	11.3 / 29.1	9.9 / 25.6	20.1 / 45.0
Fine-only (ours)	13.2 / 32.2	11.3 / 27.2	22.7 / 46.4
Coarse2Fine (ours)	12.6 / 31.3	11.1 / 27.5	22.6 / 47.3

urban area. The medium-precision localization in the urban area is affected by numerous dynamic objects. We further compare the performance on different foliage categories from [9], *Foliage* and *Mixed Foliage* with the reference database under *No Foliage*, which is the most challenging problem for this dataset. The results are shown in Table IV, from which we can see that our result is better than baselines under different conditions of foliage for the localization with medium and high precision. To investigate the performance under different weather conditions, we compare the models with baselines on the *Overcast*, *Cloudy*, and *Low Sun* conditions with the reference database under *Sunny* in Table V, which covers almost all the weather conditions. It could be seen that our results present the best medium- and high-accuracy results on most of the weather conditions. The *Cloudy* weather contains plenty of clouds in the sky, which provides some noise in the activation map for fine retrieval with reference to the clear sky under *Sunny*, which could be regarded as a kind of dynamic objects.

TABLE IV
COMPARISON WITH BASELINES ON FOLIAGE CONDITION
REFERENCE IS NO FOLIAGE

Method	Foliage (%) 0.25 m / 0.5 m 2° / 5°	Mixed Foliage (%) 0.25 m / 0.5 m 2° / 5°
FAB-MAP [74]	1.1 / 2.7	1.0 / 2.5
NetVLAD [4]	10.4 / 26.1	11.0 / 26.7
DenseVLAD [6]	13.2 / 31.6	16.2 / 38.1
DIFL-FCL [63]	13.9 / 32.7	16.6 / 38.6
Coarse-only (ours)	14.0 / 33.1	16.4 / 38.5
Fine-only (ours)	15.3 / 33.5	19.1 / 42.2
Coarse2Fine (ours)	15.2 / 34.1	18.7 / 41.7

From the results of different areas, vegetation, and weather, it can be seen that the finer retrieval boosts the results of coarse retrieval. Moreover, the coarse-to-fine retrieval strategy gives better performance than the fine-only method in some cases, showing the significance and effectiveness for high- and medium-precision localization of the two-stage strategy. The reasonable explanation for the good performance under different foliage and weather conditions lies in that the latent content code is robust and invariant for changing vegetation and illumination. All the results (including ours) are from the

TABLE V
COMPARISON WITH BASELINES ON WEATHER CONDITION
REFERENCE IS SUNNY

Method	Overcast (%) 0.25 m / 0.5 m 2° / 5°	Cloudy (%) 0.25 m / 0.5 m 2° / 5°	Low Sun (%) 0.25 m / 0.5 m 2° / 5°
FAB-MAP [74]	0.9 / 2.7	1.8 / 4.1	2.0 / 4.6
NetVLAD [4]	10.9 / 27.0	13.0 / 30.5	10.1 / 25.7
DenseVLAD [6]	15.1 / 35.2	18.4 / 41.8	15.1 / 36.9
DIFL-FCL [63]	15.9 / 36.9	16.4 / 37.6	13.9 / 34.1
Coarse-only (ours)	15.9 / 36.9	16.5 / 38.2	13.9 / 34.4
Fine-only (ours)	18.3 / 39.4	18.9 / 40.3	16.2 / 37.7
Coarse2Fine (ours)	18.0 / 39.6	18.6 / 40.5	15.8 / 37.3

official benchmark website of long-term visual localization [9]. Some results of fine-retrieval are shown in Fig. 7, where the activation maps give the localizing information of feature maps and the salient areas mostly exist around the edges or adjacent parts of different instance patches due to the gradient-based activation.

C. Evaluation on RobotCar Dataset

In order to further validate the generalization ability of our proposed method to the unseen scenarios, we directly use the pre-trained models on urban area of CMU-Seasons to test on the RobotCar dataset, according to the correspondent condition from CMU-Seasons for every query condition of RobotCar based on Table II. Considering the database images are much more than query images under each condition, the two-stage strategy is skipped for practicality and efficiency, only testing coarse-only and fine-only models. The metric for both coarse and fine retrieval is the mean value of the *cosine similarity* on the height and width dimension as shown in (16).

The comparison results are shown in Table VI, where we can see that our method outperforms other baseline methods under the *Night* and *Night-rain* conditions. Note that the model we use for the night-time retrieval is the same as the database because night-time images are not included in the training set, showing the effectiveness of the representation learning in the latent space form autoencoder-structured model. Since the images under *Night* and *Night-rain* conditions have too poor context or localizing information to find the correct similarity activation maps, the coarse model performs better than the finer model.

Our results under all the *Day* conditions are the best for high-precision performance, showing the powerful generalization ability in the unknown scenarios and environments through attaining satisfactory retrieval-based localization results. All the results (including ours) are also from the official benchmark website of long-term visual localization [9]. Some day-time results are shown in Fig. 8, including all the environments which have similar ones among pre-trained models on CMU-Seasons dataset.

D. Ablation Study

For the further ablation study in Table I, we implement different strategies (*Coarse-only*, *Fine-only*, and *Coarse-to-*

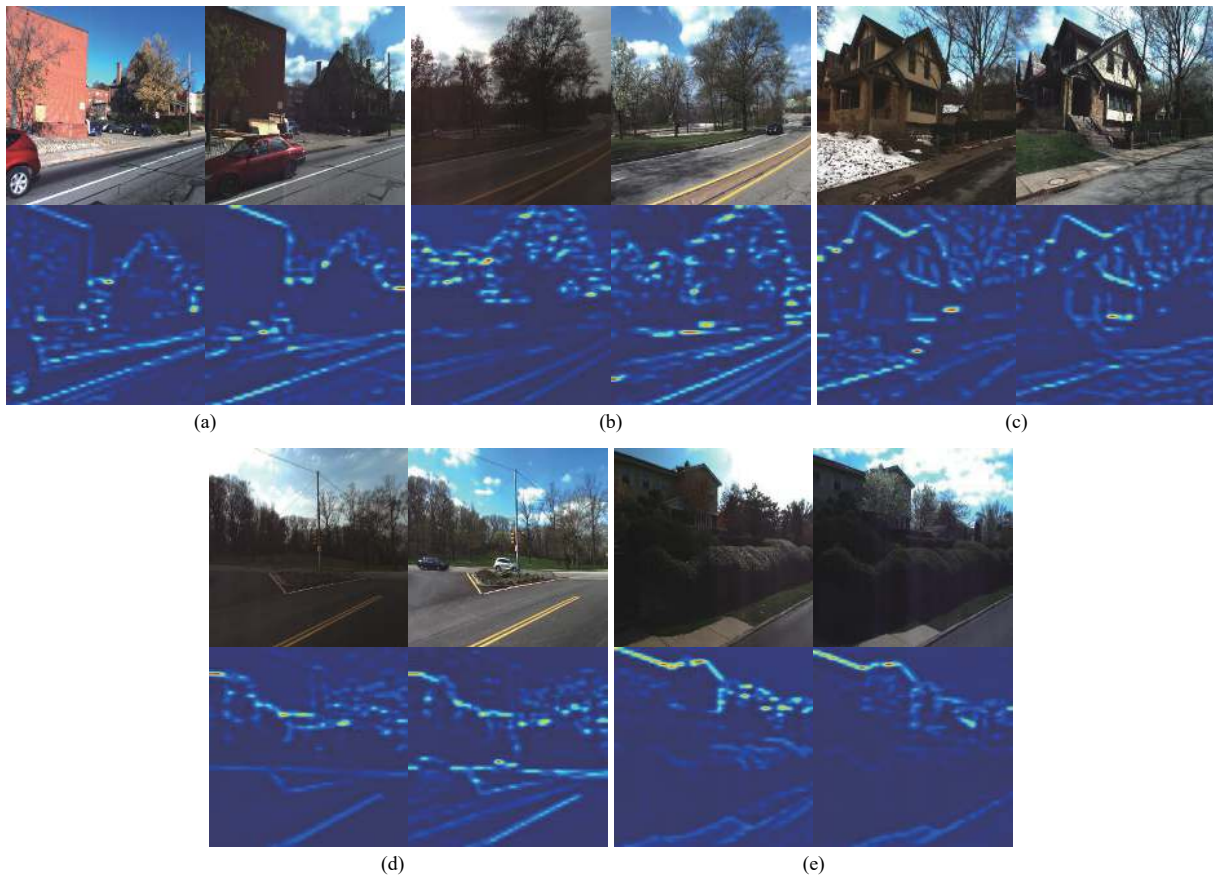


Fig. 7. Results on CMU-Seasons dataset. For each set of images in (a) to (e), the top left is the query image while the top right is the database image under the condition of *Sunny + No Foliage*. The query images of set (a) to (e) are under the conditions of *Low Sun + Mixed Foliage*, *Overcast + Mixed Foliage*, *Low Sun + Snow*, *Low Sun + Foliage* and *Sunny + Foliage*, respectively. The visualizations of similarity activation maps are on the bottom row for all the query or database RGB images.

TABLE VI
RESULTS COMPARISON TO BASELINES ON ROBOTCAR DATASET

Method	Night all (%)	Day all (%)
	0.25 m / 0.5 m 2° / 5°	0.25 m / 0.5 m 2° / 5°
FAB-MAP [74]	0.0 / 0.0	2.7 / 11.8
NetVLAD [4]	0.3 / 2.3	6.4 / 26.3
DenseVLAD [6]	1.0 / 4.4	7.6 / 31.2
DIFL+FCL [63]	2.5 / 6.5	7.6 / 26.2
Coarse-only (ours)	3.3 / 8.7	7.4 / 25.8
Fine-only (ours)	2.1 / 4.8	8.2 / 27.0

fine) and different loss terms (*FCL*, *Triplet FCL*, *SAM*, and *Triplet SAM*) during model training, and test them on CMU-Seasons dataset. The only difference between *Coarse-only* and *Fine-only* lies in whether the model is trained with *SAM* or not, while coarse-to-fine strategy follows the two-stage strategy in Section IV-C. It could be seen that *Coarse-only* models perform the best in low-precision localization, which is suitable to provide the rough candidates for the upcoming finer retrieval. With the incorporation of *SAM*-related loss, the medium- and high-precision accuracies increase while the low-precision one decreases. The *Coarse-to-fine* combines the advantages of *Coarse-only* and *Fine-only* together, improving the low-precision localization of fine models as well as the

medium- and high-precision localization of coarse models simultaneously, which shows the effectiveness and significance of the two-stage strategy by overcoming both the weaknesses. Furthermore, because of the high-quality potential candidates provided by *Coarse-only* model, some medium-precision results of *Coarse-to-fine* on the last row perform the best and other results are extremely close the best ones, which shows the promising performance of the two-stage strategy.

From the first two rows of *Coarse-only* and *Fine-only* in Table I, the *Flipped Negative* and the *Hard Negative* samples are shown to be necessary and beneficial to the final results, especially for the flipping operation for data augmentation. On the third and fourth row, the DIFL with FCL performs better than vanilla ComboGAN (3), which indicates that FCL assists to extract the domain-invariant feature. Due to the effective self-supervised triplet loss with hard negative pairs, the performance with *Triplet FCL* or *Triplet SAM* is significantly improved compared with the results on the fourth or ninth row, respectively. To validate the effectiveness of *Adaptive Margin* in triplet loss, we compare the results of *Constant Margin* and *Adaptive Margin*, which show that the model with adaptive margin gives better results than that with constant margin for both *Triplet FCL* and *Triplet SAM*. The last row in *Fine-only* strategy shows the hybrid adaptive triplet losses of both FCL and SAM are beneficial to the fine retrieval. Note

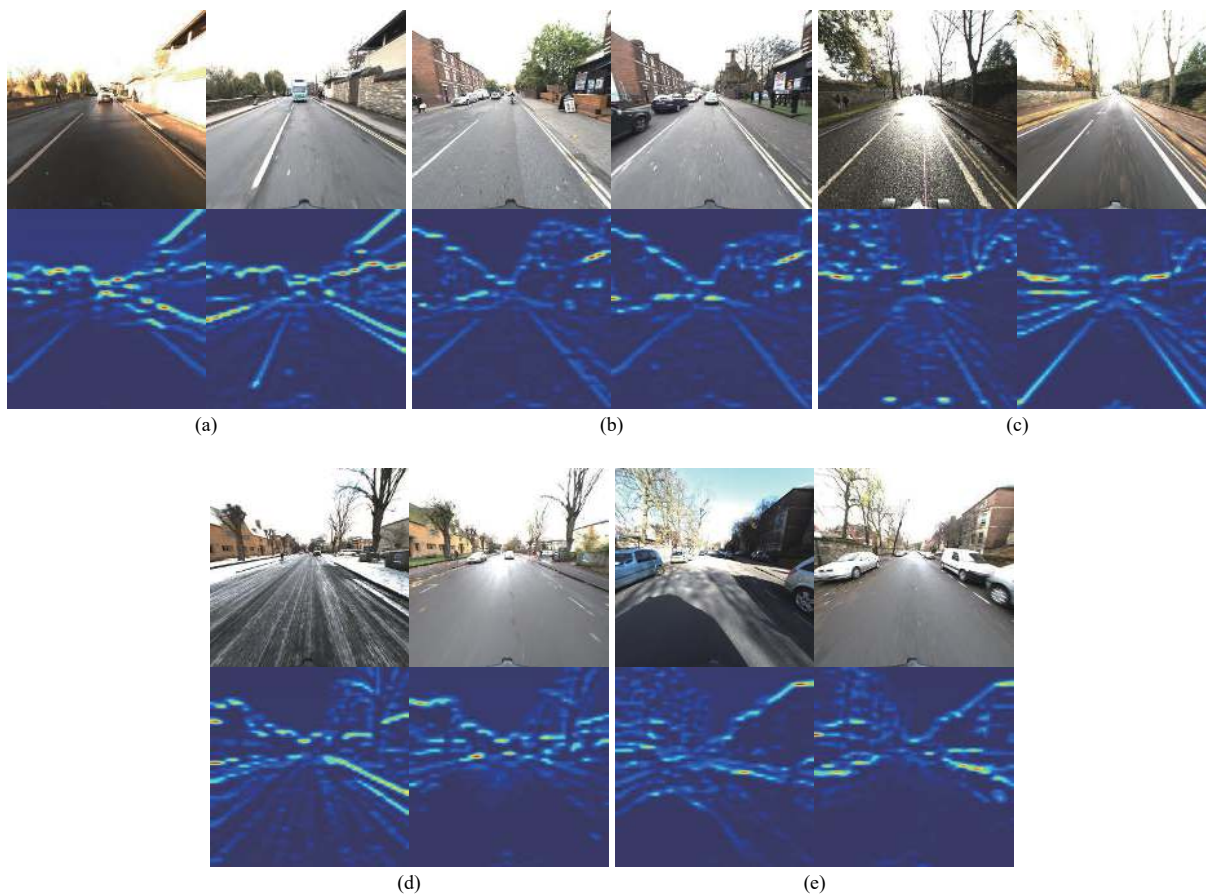


Fig. 8. Results on RobotCar dataset. For each set of images in (a) to (e), the top left is the day-time query image while the top right is the database image under the condition of *Overcast*. The query images of set (a) to (e) are under the conditions of *Dawn*, *Overcast-summer*, *Overcast-winter*, *Snow* and *Sun*, respectively. The visualizations of similarity activation maps are on the bottom row for all the query or database RGB images.

that the settings of training and testing for Table I are consistent internally, but are slightly different from the experimental settings in the [63] in many aspects, like training epochs, the metrics for retrieval, the choice of the pre-trained models for testing, etc. Also, the adaptive margin for triplet loss is partially influenced by the hard negative samples, because the less distance of negative pairs means relatively less margin to positive pairs which reduce the positive distance and the adaptive margin increases consequently.

E. Real-Site Experiment

For the real-site experiment, the dataset is collected through an AGV with ZED Stereo Camera and RTK-GPS, and mobile robot is shown as Fig. 9(a). The routine we choose is around the Lawn besides the School Building on the campus, which is around 2 km and is shown in Fig. 9(b). We collect different environments including the weather, daytime, and illumination changes, as classify them as *Sunny*, *Overcast*, and *Night*, respectively. There are 12 typical places as key frames with 25 different angles of view point for challenging localization, marked in red circles in Fig. 9(b), compensating the single perspective of driving scenes in both CMU-Seasons and Oxford RobotCar dataset. There are 300 images for each environment and some samples of the dataset are shown as Fig. 10. The same places along the routes are mainly within the distance of 5 m, which acts as the 25 groundtruth images

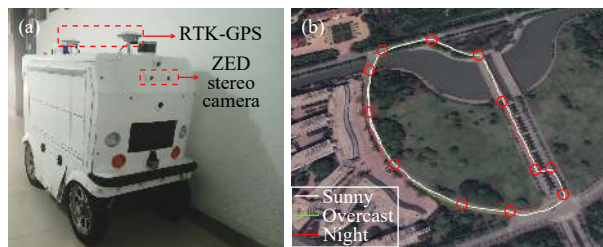


Fig. 9. Image (a) shows the mobile robot used to collect dataset with RTK-GPS and ZED Stereo Camera. Image (b) shows the routines of the dataset under changing environments, illustrated in different colored lines and the red circles indicate the 12 typical places for recognition and retrieval with different perspectives.

of place recognition from GPS data.

Since all three environments are during autumn, we use the CMU-Seasons pretrained models under *Low Sun + Mixed Foliage* for *Sunny*, *Overcast + Mixed Foliage* for *Overcast*, and *Cloudy + Mixed Foliage* for *Night* in the experiments. The three place recognition experiments are query images under *Sunny* with database under *Overcast*, query images under *Sunny* with database under *Night*, and query images under *Night* with database under *Overcast*.

For each query image, we retrieve Top- N candidates (N from 1 to 25) from the database and calculate average recall

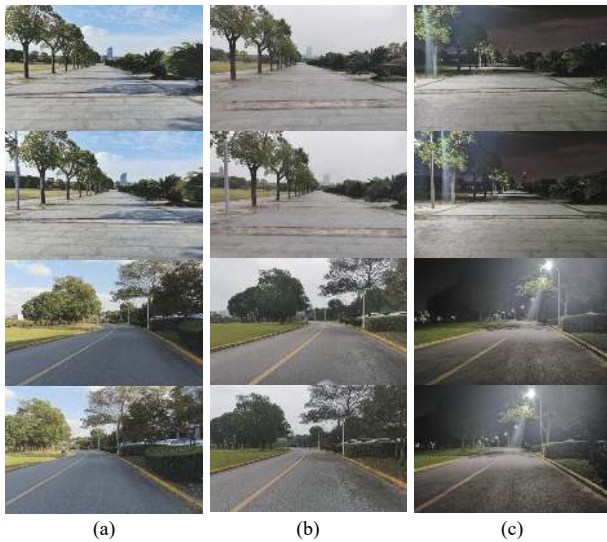


Fig. 10. Dataset images for real-site experiment. Column (a) is *Sunny*, Column (b) is *Overcast*, and Column (c) is *Night*. The first and last two rows show the changing perspectives, which gives more image candidates for the typical places.

rate to demonstrate the performance of the coarse-only and fine-only methods. For the coarse-to-fine method, first the coarse-only model retrieves the Top- $2N$ candidates ($2N$ from 2 to 50) and then the fine-only model retrieves finer Top- N candidates (N from 1 to 25) from them, the average recall is calculated over all the query images.

As shown in the Fig. 11, the results of three proposed methods are validated under three different retrieval environmental settings. From the results, it can be seen that the coarse-only method performs better than the fine-only method in the large-scale place recognition, which is consistent with the results of coarse precision on CMU-Seasons in Table I. Besides, the coarse-to-fine strategy obviously improves the performance of both coarse-only and fine-only methods, which shows that the effectiveness and applicability of the two-stage method. The coarse-to-fine performance within top 5 recall is limited by the performance of fine model, which is improved as the number of database retrieval candidates (N) increases.

Since time consumption is important for place recognition in robotic applications, we have measured the time cost of

three proposed methods in the real-site experiment. As shown in Table VII, the average time of inference is to extract the feature representation through encoder while the average time of retrieval is to retrieve top 25 out of 300 database candidates through brute-force searching in the real-site experiment. By comparing the three methods, it could be seen that although the inference time of coarse-to-fine is almost the sum of coarse-only and fine-only, the time consumption is short enough for representation extraction. For brute-force retrieval, the time of coarse-to-fine is a little bit larger than the coarse-only and fine-only methods because the second finer-retrieval stage only find top 25 out of 50 coarse candidates, which costs much less time. Note that the retrieval time cost could be significantly reduced through other ways of search, like KD-tree instead of brute-force search, but these techniques are beyond the focus of this work so Table VII only gives relative time comparison of the three proposed strategies, validating the time-efficiency and effectiveness of the two-stage method.

VI. CONCLUSION

In this work, we have formulated a domain-invariant feature learning architecture for long-term retrieval-based localization with feature consistency loss (FCL). Then a novel loss based on gradient-weighted similarity activation map (Grad-SAM) is proposed for the improvement of high-precision performance. The adaptive triplet loss based on FCL loss or Grad-SAM loss is incorporated to the framework to form the coarse or fine retrieval methods, resulting in the coarse-to-fine testing pipeline. Our proposed method is also compared with several state-of-the-art image-based localization baselines on CMU-Seasons and RobotCar-Seasons dataset, where our results outperform the baseline methods for image retrieval in medium- and high-precision localization in challenging environments. Real-site experiment validate the efficiency and effectiveness of the proposed further. However, there are a few concerns about our method that the performance under the dynamic scenes is weak compared to other image-based methods, which can be addressed by adding semantic information to enhance the robustness to dynamic objects in the future. Another concern lies in the unified model for robust visual localization where the front-end network collaborate with representation learning better.

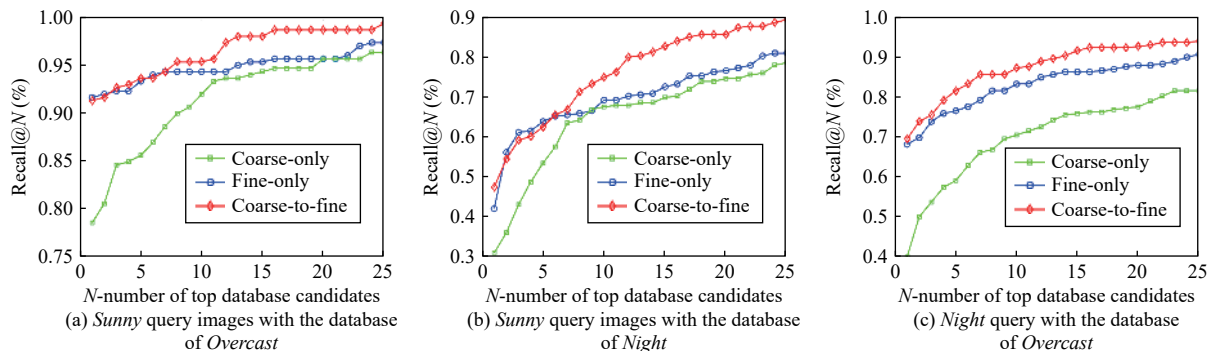


Fig. 11. Results of the real site experiment. (a) is the result of *Sunny* query images with the database of *Overcast*; (b) is the result of *Sunny* query images with the database of *Night*; (c) is the result of *Night* query images with the database of *Overcast*.

TABLE VII
TIME CONSUMPTION OF DIFFERENT METHODS

Method	Time of inference (ms)	Time of brute-force retrieval (s)
Coarse-only	1.2	0.81
Fine-only	1.3	0.78
Coarse-to-fine	2.3	0.89

ACKNOWLEDGMENT

The authors would like to thank Zhijian Qiao from Department of Automation at Shanghai Jiao Tong University for his contribution to the real-site experiments including the collection of dataset and the comparison experiments.

REFERENCES

- [1] T. Sattler, B. Leibe, and L. Kobbelt, "Efficient & effective prioritized matching for large-scale image-based localization," *IEEE Trans. Pattern Anal. Mach. Intell.*, vol. 39, no. 9, pp. 1744–1756, Sept. 2017.
- [2] B. Bescos, J. M. Fácil, J. Civera, and J. Neira, "DynaSLAM: Tracking, mapping, and inpainting in dynamic scenes," *IEEE Robot. Autom. Lett.*, vol. 3, no. 4, pp. 4076–4083, Oct. 2018.
- [3] L. P. Wang and H. Wei, "Avoiding non-Manhattan obstacles based on projection of spatial corners in indoor environment," *IEEE/CAA J. Autom. Sinica*, vol. 7, no. 4, pp. 1190–1200, Jul. 2020.
- [4] R. Arandjelovic, P. Gronat, A. Torii, T. Pajdla, and J. Sivic, "NetVLAD: CNN architecture for weakly supervised place recognition," *IEEE Trans. Pattern Anal. Mach. Intell.*, vol. 40, no. 6, pp. 1437–1451, Jun. 2018.
- [5] S. Lowry, N. Sünderhauf, P. Newman, J. J. Leonard, D. Cox, P. Corke, and M. J. Milford, "Visual place recognition: A survey," *IEEE Trans. Robot.*, vol. 32, no. 1, pp. 1–19, Feb. 2016.
- [6] A. Torii, R. Arandjelovic, J. Sivic, M. Okutomi, and T. Pajdla, "4/7 place recognition by view synthesis," *IEEE Trans. Pattern Anal. Mach. Intell.*, vol. 40, no. 2, pp. 257–271, Feb. 2018.
- [7] T. Sattler, Q. J. Zhou, M. Pollefeys, and L. Leal-Taixé, "Understanding the limitations of CNN-based absolute camera pose regression," in *Proc. IEEE/CVF Conf. Computer Vision and Pattern Recognition*, Long Beach, CA, USA, 2019, pp. 3297–3307.
- [8] P. E. Sarlin, C. Cadena, R. Siegwart, and M. Dymczyk, "From coarse to fine: Robust hierarchical localization at large scale," in *Proc. IEEE/CVF Conf. Computer Vision and Pattern Recognition*, Long Beach, CA, USA, 2019, pp. 12708–12717.
- [9] T. Sattler, W. Maddern, C. Toft, *et al.*, "Benchmarking 6DOF outdoor visual localization in changing conditions," in *Proc. IEEE/CVF Conf. Computer Vision and Pattern Recognition*, Salt Lake City, UT, USA, 2018, pp. 8601–8610.
- [10] Y. F. Ma, Z. Y. Wang, H. Yang, and L. Yang, "Artificial intelligence applications in the development of autonomous vehicles: A survey," *IEEE/CAA J. Autom. Sinica*, vol. 7, no. 2, pp. 315–329, Mar. 2020.
- [11] D. Doan, Y. Latif, T. J. Chin, Y. Liu, T. T. Do, and I. Reid, "Scalable place recognition under appearance change for autonomous driving," in *Proc. IEEE/CVF Int. Conf. Computer Vision*, Seoul, Korea (South), 2019, pp. 9318–9327.
- [12] P. Yin, L. Y. Xu, X. Q. Li, C. Yin, Y. L. Li, R. A. Srivatsan, L. Li, J. M. Ji, and Y. Q. He, "A multi-domain feature learning method for visual place recognition," in *Proc. IEEE Int. Conf. Robotics and Automation*, Montreal, QC, Canada, 2019, pp. 319–324.
- [13] Z. T. Chen, A. Jacobson, N. Sünderhauf, B. Upcroft, L. Q. Liu, C. H. Shen, I. Reid, and M. Milford, "Deep learning features at scale for visual place recognition," in *Proc. IEEE Int. Conf. Robotics and Automation*, Singapore, 2017, pp. 3223–3230.
- [14] J. Wang, Y. Song, T. Leung, C. Rosenberg, J. B. Wang, J. Philbin, B. Chen, and Y. Wu, "Learning fine-grained image similarity with deep ranking," in *Proc. IEEE Conf. Computer Vision and Pattern Recognition*, Columbus, OH, USA, 2014, pp. 1386–1393.
- [15] P. Wohlhart and V. Lepetit, "Learning descriptors for object recognition and 3D pose estimation," in *Proc. IEEE Conf. Computer Vision and Pattern Recognition*, Boston, MA, USA, 2015, pp. 3109–3118.
- [16] J. W. Lu, J. L. Hu, and Y. P. Tan, "Discriminative deep metric learning for face and kinship verification," *IEEE Trans. Image Process.*, vol. 26, no. 9, pp. 4269–4282, Sept. 2017.
- [17] S. Lowry and M. J. Milford, "Supervised and unsupervised linear learning techniques for visual place recognition in changing environments," *IEEE Trans. Robot.*, vol. 32, no. 3, pp. 600–613, Jun. 2016.
- [18] A. Gordo, J. Almazán, J. Revaud, and D. Larlus, "End-to-end learning of deep visual representations for image retrieval," *Int. J. Comput. Vis.*, vol. 124, no. 2, pp. 237–254, Sept. 2017.
- [19] F. Radenović, G. Tolias, and O. Chum, "Fine-tuning CNN image retrieval with no human annotation," *IEEE Trans. Pattern Anal. Mach. Intell.*, vol. 41, no. 7, pp. 1655–1668, Jul. 2019.
- [20] B. L. Zhou, A. Khosla, A. Lapedriza, A. Oliva, and A. Torralba, "Learning deep features for discriminative localization," in *Proc. IEEE Conf. Computer Vision and Pattern Recognition*, Las Vegas, NV, USA, 2016, pp. 2921–2929.
- [21] R. R. Selvaraju, M. Cogswell, A. Das, R. Vedantam, D. Parikh, and D. Batra, "Grad-CAM: Visual explanations from deep networks via gradient-based localization," in *Proc. IEEE Int. Conf. Computer Vision*, Venice, Italy, 2017, pp. 618–626.
- [22] A. Chattopadhyay, A. Sarkar, P. Howlader, and V. N. Balasubramanian, "Grad-CAM++: Generalized gradient-based visual explanations for deep convolutional networks," in *Proc. IEEE Winter Conf. Applications of Computer Vision*, Lake Tahoe, NV, USA, 2018, pp. 839–847.
- [23] H. J. Kim, E. Dunn, and J. M. Frahm, "Learned contextual feature reweighting for image geo-localization," in *Proc. IEEE Conf. Computer Vision and Pattern Recognition*, Honolulu, HI, USA, 2017, pp. 3251–3260.
- [24] Z. T. Chen, L. Q. Liu, I. Sa, Z. Y. Ge, and M. Chli, "Learning context flexible attention model for long-term visual place recognition," *IEEE Robot. Autom. Lett.*, vol. 3, no. 4, pp. 4015–4022, Oct. 2018.
- [25] H. Y. Gu, H. S. Wang, F. Xu, Z. Liu, and W. D. Chen, "Active fault detection of soft manipulator in visual servoing," *IEEE Trans. Ind. Electron.*, 2020. DOI: 10.1109/TIE.2020.3028813
- [26] L. J. Han, H. S. Wang, Z. Liu, W. D. Chen, and X. F. Zhang, "Vision-based cutting control of deformable objects with surface tracking," *IEEE/ASME Trans. Mechatron.*, 2020. DOI: 10.1109/TMECH.2020.3029114
- [27] D. Gálvez-López and J. D. Tardos, "Bags of binary words for fast place recognition in image sequences," *IEEE Trans. Robot.*, vol. 28, no. 5, pp. 1188–1197, Oct. 2012.
- [28] W. Shi, P. X. Liu, and M. H. Zheng, "A mixed-depth visual rendering method for bleeding simulation," *IEEE/CAA J. Autom. Sinica*, vol. 6, no. 4, pp. 917–925, Jul. 2019.
- [29] Z. Y. Liu and H. Qiao, "GNCCP-graduated NonConvexity and concavity procedure," *IEEE Trans. Pattern Anal. Mach. Intell.*, vol. 36, no. 6, pp. 1258–1267, Jun. 2014.
- [30] H. Qiao, Y. L. Li, T. Tang, and P. Wang, "Introducing memory and association mechanism into a biologically inspired visual model," *IEEE Trans. Cybernet.*, vol. 44, no. 9, pp. 1485–1496, Sept. 2014.
- [31] R. Mur-Artal and J. D. Tardós, "ORB-SLAM2: An open-source SLAM system for monocular, stereo, and RGB-D cameras," *IEEE Trans. Robot.*, vol. 33, no. 5, pp. 1255–1262, Oct. 2017.
- [32] H. Jégou, M. Douze, C. Schmid, and P. Pérez, "Aggregating local descriptors into a compact image representation," in *Proc. IEEE Computer Society Conf. Computer Vision & Pattern Recognition*, San Francisco, CA, USA, 2010, pp. 3304–3311.
- [33] M. J. Milford and G. F. Wyeth, "SeqSLAM: Visual route-based navigation for sunny summer days and stormy winter nights," in *Proc.*

- IEEE Int. Conf. Robotics and Automation*, Saint Paul, MN, USA, 2012, pp. 1643–1649.
- [34] S. M. Siam and H. Zhang, “Fast-SeqSLAM: A fast appearance based place recognition algorithm,” in *Proc. IEEE Int. Conf. Robotics and Automation*, Singapore, 2017, pp. 5702–5708.
- [35] Y. Xing, C. Lv, L. Chen, H. J. Wang, H. Wang, D. P. Cao, E. Velenis, and F. Y. Wang, “Advances in vision-based lane detection: Algorithms, integration, assessment, and perspectives on ACP-based parallel vision,” *IEEE/CAA J. Autom. Sinica*, vol. 5, no. 3, pp. 645–661, May 2018.
- [36] T. Jenicek and O. Chum, “No fear of the dark: Image retrieval under varying illumination conditions,” in *Proc. IEEE/CVF Int. Conf. Computer Vision*, Seoul, Korea (South), 2019, pp. 9696–9703.
- [37] P. Isola, J. Y. Zhu, T. H. Zhou, and A. A. Efros, “Image-to-image translation with conditional adversarial networks,” in *Proc. IEEE Conf. Computer Vision and Pattern Recognition*, Honolulu, HI, USA, 2017, pp. 5967–5976.
- [38] A. Anoosheh, E. Agustsson, R. Timofte, and L. Van Gool, “ComboGAN: Unrestrained scalability for image domain translation,” in *Proc. IEEE/CVF Conf. Computer Vision and Pattern Recognition Workshops*, Salt Lake City, UT, USA, 2018, pp. 896–903.
- [39] M. Y. Liu, T. Breuel, and J. Kautz, “Unsupervised image-to-image translation networks,” in *Proc. 31st Int. Conf. Neural Information Processing Systems*, Red Hook, NY, United States, 2017, pp. 700–708.
- [40] X. Huang, M. Y. Liu, S. Belongie, and J. Kautz, “Multimodal unsupervised image-to-image translation,” in *Proc. European Conf. Computer Vision*, Munich, Germany, 2018, pp. 179–196.
- [41] I. Goodfellow, J. Pouget-Abadie, M. Mirza, B. Xu, D. Warde-Farley, S. Ozair, A. Courville, and Y. Bengio, “Generative adversarial nets,” in *Proc. 27th Int. Conf. Neural Information Processing Systems*, Cambridge, MA, United States, 2014, pp. 2672–2680.
- [42] A. Radford, L. Metz, and S. Chintala, “Unsupervised representation learning with deep convolutional generative adversarial networks,” arXiv preprint arXiv: 1511.06434, 2015.
- [43] H. Porav, W. Maddern, and P. Newman, “Adversarial training for adverse conditions: Robust metric localisation using appearance transfer,” in *Proc. IEEE Int. Conf. Robotics and Automation*, Brisbane, QLD, Australia, 2018, pp. 1011–1018.
- [44] J. Y. Zhu, T. Park, P. Isola, and A. A. Efros, “Unpaired image-to-image translation using cycle-consistent adversarial networks,” in *Proc. IEEE Int. Conf. Computer Vision*, Venice, Italy, 2017, pp. 2242–2251.
- [45] A. Anoosheh, T. Sattler, R. Timofte, M. Pollefeys, and L. Van Gool, “Night-to-day image translation for retrieval-based localization,” in *Proc. IEEE Int. Conf. Robotics and Automation*, Montreal, QC, Canada, 2019, pp. 5958–5964.
- [46] T. Naseer, G. L. Oliveira, T. Brox, and W. Burgard, “Semantics-aware visual localization under challenging perceptual conditions,” in *Proc. IEEE Int. Conf. Robotics and Automation*, Singapore, 2017, pp. 2614–2620.
- [47] E. Stenborg, C. Toft, and L. Hammarstrand, “Long-term visual localization using semantically segmented images,” in *Proc. IEEE Int. Conf. Robotics and Automation*, Brisbane, QLD, Australia, 2018, pp. 6484–6490.
- [48] N. Piasco, D. Sidibé, V. Gouet-Brunet, and C. Demonceaux, “Learning scene geometry for visual localization in challenging conditions,” in *Proc. IEEE Int. Conf. Robotics and Automation*, Montreal, QC, Canada, 2019, pp. 9094–9100.
- [49] N. Piasco, D. Sidibé, V. Gouet-Brunet, and C. Demonceaux, “Improving image description with auxiliary modality for visual localization in challenging conditions,” *Int. J. Comput. Vis.*, 2021, DOI: 10.1007/s11263-020-01363-6
- [50] X. H. Wang and H. B. Duan, “Hierarchical visual attention model for saliency detection inspired by avian visual pathways,” *IEEE/CAA J. Autom. Sinica*, vol. 6, no. 2, pp. 540–552, Mar. 2019.
- [51] Z. Xin, Y. H. Cai, T. Lu, X. X. Xing, S. J. Cai, J. P. Zhang, Y. P. Yang, and Y. Q. Wang, “Localizing discriminative visual landmarks for place recognition,” in *Proc. IEEE Int. Conf. Robotics and Automation*, Montreal, QC, Canada, 2019, pp. 5979–5985.
- [52] X. Luo, D. X. Wang, M. C. Zhou, and H. Q. Yuan, “Latent factor-based recommenders relying on extended stochastic gradient descent algorithms,” *IEEE Trans. Syst. Man Cybernet.: Syst.*, vol. 51, no. 2, pp. 916–926, 2019.
- [53] D. Wu, Q. He, X. Luo, M. S. Shang, Y. He, and G. Y. Wang, “A posterior-neighborhood-regularized latent factor model for highly accurate web service QoS prediction,” *IEEE Trans. Serv. Comput.*, 2019. DOI: 10.1109/TSC.2019.2961895
- [54] D. Wu, X. Luo, M. S. Shang, Y. He, G. Y. Wang, and M. C. Zhou, “A deep latent factor model for high-dimensional and sparse matrices in recommender systems,” *IEEE Trans. Syst. Man Cybernet.: Syst.*, 2019. DOI: 10.1109/TSMC.2019.2931393
- [55] R. Gong, W. Li, Y. H. Chen, and L. Van Gool, “DLOW: Domain flow for adaptation and generalization,” in *Proc. IEEE/CVF Conf. Computer Vision and Pattern Recognition*, Long Beach, CA, 2019, pp. 2472–2481.
- [56] A. Achille and S. Soatto, “Emergence of invariance and disentanglement in deep representations,” in *Proc. Information Theory and Applications Workshop*, San Diego, CA, USA, 2018, pp. 1–9.
- [57] H. Kim and A. Mnih, “Disentangling by factorising,” in *Proc. 35th Int. Conf. Machine Learning*, Stockholm, Sweden, 2018, pp. 2649–2658.
- [58] A. Makhzani, J. Shlens, N. Jaitly, I. Goodfellow, and B. Frey, “Adversarial autoencoders,” arXiv preprint arXiv: 1511.05644, 2015.
- [59] M. Mathieu, J. B. Zhao, P. Sprechmann, A. Ramesh, and Y. LeCun, “Disentangling factors of variation in deep representations using adversarial training,” in *Proc. 30th Int. Conf. Neural Information Processing Systems*, Red Hook, NY, United States, 2016, pp. 5047–5055.
- [60] X. Chen, Y. Duan, R. Houthoof, J. Schulman, I. Sutskever, and P. Abbeel, “InfoGAN: Interpretable representation learning by information maximizing generative adversarial nets,” in *Proc. 30th Int. Conf. Neural Information Processing Systems*, Red Hook, NY, United States, 2016, pp. 2180–2188.
- [61] C. Donahue, Z. C. Lipton, A. Balsubramani, and J. McAuley, “Semantically decomposing the latent spaces of generative adversarial networks,” arXiv preprint arXiv: 1705.07904, 2018.
- [62] M. Lopez-Antequera, R. Gomez-Ojeda, N. Petkov, and J. Gonzalez-Jimenez, “Appearance-invariant place recognition by discriminatively training a convolutional neural network,” *Pattern Recogn. Lett.*, vol. 92, pp. 89–95, Jun. 2017.
- [63] H. J. Hu, H. S. Wang, Z. Liu, C. G. Yang, W. D. Chen, and L. Xie, “Retrieval-based localization based on domain-invariant feature learning under changing environments,” in *Proc. IEEE/RSJ Int. Conf. Intelligent Robots and Systems*, Macau, China, 2019, pp. 3684–3689.
- [64] L. Tang, Y. Wang, Q. H. Luo, X. Q. Ding, and R. Xiong, “Adversarial feature disentanglement for place recognition across changing appearance,” in *Proc. IEEE Int. Conf. Robotics and Automation*, Paris, France, 2020, pp. 1301–1307.
- [65] S. Hausler, A. Jacobson, and M. Milford, “Filter early, match late: Improving network-based visual place recognition,” in *Proc. IEEE/RSJ Int. Conf. Intelligent Robots and Systems*, Macau, China, 2019, pp. 3268–3275.
- [66] S. Garg, N. Suenderhauf, and M. Milford, “Don’t look back: Robustifying place categorization for viewpoint- and condition-invariant place recognition,” in *Proc. IEEE Int. Conf. Robotics and Automation*, Brisbane, QLD, Australia, 2018, pp. 3645–3652.
- [67] H. Oh Song, Y. Xiang, S. Jegelka, and S. Savarese, “Deep metric learning via lifted structured feature embedding,” in *Proc. IEEE Conf. Computer Vision and Pattern Recognition*, Las Vegas, NV, USA, 2016, pp. 4004–4012.
- [68] E. P. Xing, A. Y. Ng, M. I. Jordan, and S. Russell, “Distance metric learning, with application to clustering with side-information,” in *Proc.*

15th Int. Conf. Neural Information Processing Systems, Cambridge, MA, United States, 2002, pp. 521–528.

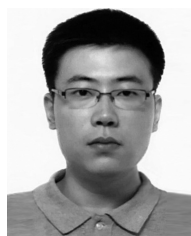
- [69] K. Q. Weinberger and L. K. Saul, “Fast solvers and efficient implementations for distance metric learning,” in *Proc. 25th Int. Conf. Machine Learning*, Helsinki, Finland, 2008, pp. 1160–1167.
- [70] R. R. Varior, M. Haloi, and G. Wang, “Gated siamese convolutional neural network architecture for human re-identification,” in *Proc. European Conf. Computer Vision*, Amsterdam, The Netherlands, 2016, pp. 791–808.
- [71] V. Balntas, S. D. Li, and V. Prisacariu, “RelocNet: Continuous metric learning relocalisation using neural nets,” in *Proc. European Conf. Computer Vision*, Munich, Germany, 2018, pp. 782–799.
- [72] E. Hoffer and N. Ailon, “Deep metric learning using triplet network,” in *Proc. Int. Workshop on Similarity-Based Pattern Recognition*, Copenhagen, Denmark, 2015, pp. 84–92.
- [73] B. G. V. Kumar, G. Carneiro, and I. Reid, “Learning local image descriptors with deep siamese and triplet convolutional networks by minimizing global loss functions,” in *Proc. IEEE Conf. Computer Vision and Pattern Recognition*, Las Vegas, NV, USA, 2016, pp. 5385–5394.
- [74] M. Cummins and P. Newman, “Fab-map: Probabilistic localization and mapping in the space of appearance,” *Int. J. Robot. Res.*, vol. 27, no. 6, pp. 647–665, Jun. 2008.
- [75] H. Badino, D. Huber, and T. Kanade, “Visual topometric localization,” in *Proc. IEEE Intelligent Vehicles Symp.*, 2011. DOI: [10.1109/IVS.2011.5940504](https://doi.org/10.1109/IVS.2011.5940504).
- [76] W. Maddern, G. Pascoe, C. Linegar, and P. Newman, “1 year, 1000 km: The Oxford RobotCar dataset,” *Int. J. Robot. Res.*, vol. 36, no. 1, pp. 3–15, Jan. 2017.



Hanjiang Hu received the B.Eng degree in mechanical engineering from Shanghai Jiao Tong University in 2018. He is currently working toward the M.S. degree in control science and engineering at Shanghai Jiao Tong University. His current research interests include visual perception and localization, autonomous driving, computer vision and machine learning.



Hesheng Wang (Senior Member, IEEE) received the B.Eng. degree in electrical engineering from the Harbin Institute of Technology in 2002, and the M.Phil. and Ph.D. degrees in automation and computer-aided engineering from The Chinese University of Hong Kong, China, in 2004 and 2007, respectively. He was a Post-Doctoral Fellow and Research Assistant with the Department of Mechanical and Automation Engineering, The Chinese University of Hong Kong, China, from 2007 to 2009. He is currently a Professor with the Department of Automation, Shanghai Jiao Tong University. His current research interests include visual servoing, service robot, adaptive robot control, and autonomous driving. Dr. Wang is an Associate Editor of *Assembly Automation and the International Journal of Humanoid Robotics*, a Technical Editor of the *IEEE/ASME Transactions on Mechatronics*. He served as an Associate Editor of the *IEEE Transactions on Robotics* from 2015 to 2019. He was the General Chair of the IEEE RCAR 2016, and the Program Chair of the IEEE ROBIO 2014 and IEEE/ASME AIM 2019.



Zhe Liu received the B.S. degree in automation from Tianjin University in 2010, and the Ph.D. degree in control technology and control engineering from Shanghai Jiao Tong University in 2016. From 2017 to 2020, he was a Post-Doctoral Fellow with the Department of Mechanical and Automation Engineering, The Chinese University of Hong Kong, China. He is currently a Research Associate with the Department of Computer Science and Technology, University of Cambridge, UK. His research interests include autonomous mobile robot, multirobot cooperation and autonomous driving system.



Weidong Chen (Member, IEEE) received the B.S. and M.S. degrees in control engineering in 1990 and 1993, and the Ph.D. degree in mechatronics in 1996, respectively, all from the Harbin Institute of Technology. Since 1996, he has been at the Shanghai Jiao Tong University where he is currently Professor of the Department of Automation, and Deputy Dean of the Institute of Medical Robotics. He is the Founder of the Autonomous Robot Laboratory. From 2013 to 2019, he served as Chair of the Department of Automation. His current research interests include perception and control of robotic systems, multi-robot systems and medical robotics.